Cell Reports

A striatal SOM-driven ChAT-iMSN loop generates beta oscillations and produces motor deficits

Graphical abstract

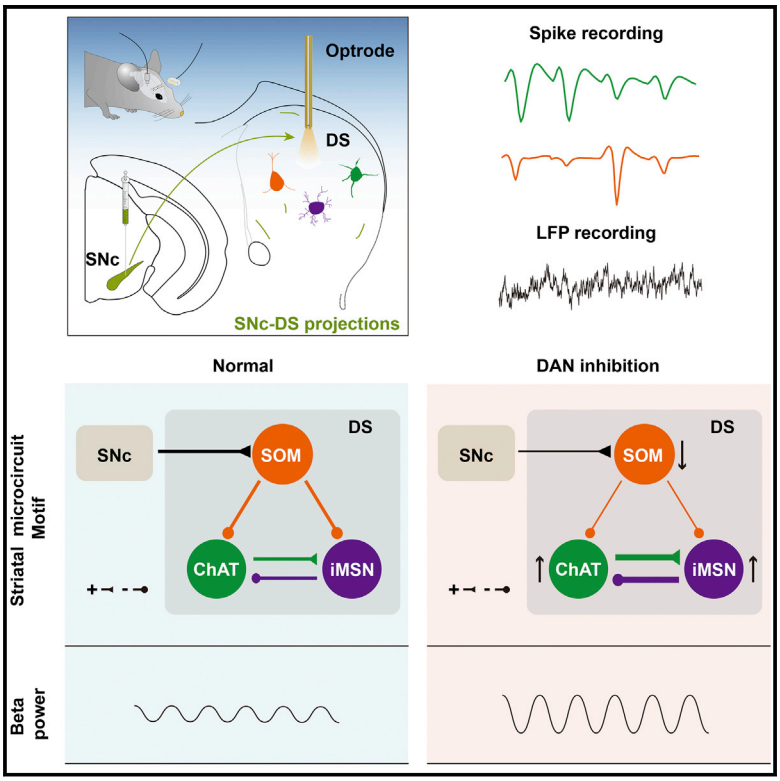

Highlights

- Inhibition of DANs selectively enhances beta oscillations and produces motor deficits
- SOMs function as the downstream effectors for DANs in beta oscillation generation
- The amplified beta power originates from a striatal SOM-driven ChAT-iMSN loop
- Closed-loop inhibition iMSNs or ChATs reduces beta power and improves motor deficits

Authors

Dandan Qian, Wei Li, Jinwen Xue, ..., Ti-Fei Yuan, Douglas Zhou, Wei Lu

Correspondence

zdz@sjtu.edu.cn (D.Z.),
luwei@seu.edu.cn (W.L.)

In brief

Qian et al. demonstrate that photoinhibition of substantia nigra pars compacta (SNc) dopaminergic terminals in striatum enhances beta oscillations, accompanied by impairment in locomotion. Specifically, the enhancement in beta power originates from a loop circuit driven by somatostatin interneurons and constituted by cholinergic interneuron and D2R medium spiny neurons.

Qian et al., 2022, Cell Reports *40*, 111111
July 19, 2022
https://doi.org/10.1016/j.celrep.2022.111111

Cell Reports

CellPress
OPEN ACCESS

Report

A striatal SOM-driven ChAT-iMSN loop generates beta oscillations and produces motor deficits

Dandan Qian,[1,7] Wei Li,[1,7] Jinwen Xue,[1,7] Yi Wu,[4,7] Ziling Wang,[6] Tao Shi,[6] Songting Li,[6] Jingxuan Yang,[1] Shi Qiu,[1] Shaoli Wang,[1,2] Yousheng Shu,[2] Liang Chen,[2] Qiao Wang,[4] Ti-Fei Yuan,[5] Douglas Zhou,[6,*] and Wei Lu[1,2,3,8,*]

[1]Minister of Education (MOE) Key Laboratory of Developmental Genes and Human Disease, School of Life Science and Technology, Southeast University, Nanjing, Jiangsu Province 210096, China

[2]Department of Neurosurgery, Huashan Hospital, Institute for Translational Brain Research, State Key Laboratory of Medical Neurobiology, MOE Frontiers Center for Brain Science, Fudan University, Shanghai 200032, China

[3]Co-innovation Center of Neuroregeneration, Nantong University, Nantong, Jiangsu Province 226001, China

[4]School of Information Science and Engineering and Yau Shing-Tung Center, Southeast University, Nanjing 210096, China

[5]Shanghai Key Laboratory of Psychotic Disorders, Shanghai Mental Health Center, Shanghai Jiaotong University School of Medicine, Shanghai 200030, China

[6]School of Mathematical Sciences, Ministry of Education-Key Laboratory of Scientific and Engineering Computing and Shanghai Frontier Science Center of Modern Analysis, Institute of Natural Sciences, Shanghai Jiao Tong University, Shanghai 200240, China

[7]These authors contributed equally

[8]Lead contact

*Correspondence: zdz@sjtu.edu.cn (D.Z.), luwei@seu.edu.cn (W.L.)

https://doi.org/10.1016/j.celrep.2022.111111

SUMMARY

Enhanced beta oscillations within the cortico-basal ganglia-thalamic (CBT) network are correlated with motor deficits in Parkinson's disease (PD), whose generation has been associated recently with amplified network dynamics in the striatum. However, how distinct striatal cell subtypes interact to orchestrate beta oscillations remains largely unknown. Here, we show that optogenetic suppression of dopaminergic control over the dorsal striatum (DS) elevates the power of local field potentials (LFPs) selectively at beta band (12–25 Hz), accompanied by impairments in locomotion. The amplified beta power originates from a striatal loop driven by somatostatin-expressing (SOM) interneurons and constituted by choline acetyltransferase (ChAT)-expressing interneurons and dopamine D2 receptor (D2R)-expressing medium spiny neurons (iMSNs). Moreover, closed-loop intervention selectively targeting striatal iMSNs or ChATs diminishes beta oscillations and restores motor function. Thus, we reveal a striatal microcircuit motif that underlies beta oscillation generation and accompanied motor deficits upon perturbation of dopaminergic control over the striatum.

INTRODUCTION

Excessive beta oscillations (12–35 Hz) within the cortico-basal ganglia-thalamic (CBT) neural network are significantly correlated with hypokinetic symptoms in motor diseases such as Parkinson's disease (PD) (Brazhnik et al., 2016; Brown, 2007; but see Leblois et al., 2007 and Willard et al., 2019). Given the clear link between motor deficits and excessive beta oscillations, understanding the origin and precise microcircuits responsible for these beta oscillations within the motor circuit is highly important for uncovering more about motor deficit pathologies. However, the exact generation process of beta oscillations remains elusive.

In PD, excessive beta oscillations are proposed to be caused by the core pathology of this disease: the loss of midbrain dopaminergic neurons (DANs). A decrease in midbrain dopamine level enhances beta oscillation power and coherence in PD animals (Mallet et al., 2008; Sharott et al., 2005). Since the striatum receives major and direct projections from DANs in the substantia nigra pars compacta (SNc) and ventral tegmental area, loss of dopamine in PD pathology would likely interrupt normal neural dynamics in the striatum (Zemel et al., 2022). Indeed, it has been demonstrated that acute local inhibition of dopaminergic projection within the striatum elevates striatal beta oscillations, indicating the importance of striatal involvements in the generation of excessive beta oscillations (Costa et al., 2006).

Recent evidence have emerged to support the striatum as a generation site for beta oscillations (Berke, 2008; Tepper and Bolam, 2004). Striatal MSNs not only project to other brain regions but also actively interact with various types of striatal interneurons, which may coordinately contribute to the generation of beta oscillations (Chuhma et al., 2011; Sharott et al., 2017; Steiner and Tseng, 2017). Previous studies have also demonstrated the involvement of striatal choline acetyltransferases (ChATs) in beta oscillation generation (McCarthy et al., 2011; Kondabolu et al., 2016). These results point to the notion that the amplification of normal striatal microcircuit dynamics may underlie the enhanced beta frequency oscillations in PD.

In the present study, we focused on the role of the striatum in the generation of beta oscillations and revealed supporting

circuitry mechanisms. Our results support a somatostatin (SOM)-driven ChAT-interneuron and D2R medium spiny neuron (iMSN) loop for the generation of beta oscillations and motor deficits.

RESULTS

Acute inhibition of dopaminergic control over striatum generates beta oscillations and produces motor deficits

We determined whether excessive beta oscillations could be generated by acutely inhibiting SNc activity. *In vivo* multi-channel local field potential (LFP) recordings was performed at the dorsal striatum (DS) in freely behaving mice (Figure S1A). Optic fiber was implanted into ipsilateral SNc for photoinhibition of striatal DANs (Figures S1B and S2A). The two-virus approach was used as previously reported (Dogbevia et al., 2016). In brief, two high-titer viruses (rAAV2/9-TH-Cre and rAAV2/9-EF1α--DIO-eNpHR3.0-EYFP) were mixed 1:2 for stereotactic injection into SNc to specifically express halorhodopsin from *Natronomonas* (NpHR) in DANs (Stauffer et al., 2016; Figures S1C–S1E). Following a 5-min baseline period, yellow light stimuli (593 nm) were delivered continuously for 1 min and repeated 3 times with 1-min intervals (Figure S1F). We found that this photoinhibition of SNc DANs led to an increase in the amplitude of beta power (12–25 Hz), reflected by the power spectrogram of LFP data recorded from DS (Figures S1G and S1H).

Optogenetic manipulation of SNc DANs decreased the firing frequency of DANs from 10.55 to 6.93 Hz (Figure 1A). To manipulate the activity of DANs targeting DS more directly (Figure 1B), in a separate set of experiments, we inhibited the SNc-DS projection terminals to see how it would affect brain oscillations in DS. The optrode was placed just above the DS and applied for both optogenetic manipulation and LFP recording at DS (Figure S2B). Very similar results were obtained in the terminal stimulation experiments (Figures 1C and 1D). In contrast, laser illumination in control mice injected with TH-Cre and EF1α-DIO-EYFP (no NpHR) failed to alter oscillation power at any frequency (Figure 1D), confirming that the observed changes in mice were due to the deactivation of DAN axon terminals. In addition, the deactivation of SNc-DS projections significantly reduced the total traveled distance resulting from increased immobility (Figures 1E–1H). These results indicate that suppressing the nigro-striatal terminal is sufficient to elicit excessive beta oscillations and motor deficits.

Activity changes in striatal cell subtypes during photoinhibition of SNc-DS projections

To dissect the potential microcircuits that underlie the alterations in LFP and movement, we investigated how the activities of different cell types in DS were changed following the photoinhibition of SNc dopaminergic terminals in DS. For this purpose, we targeted all types of neurons except parvalbumin (PV) interneurons with channelrhodopsin-2 (ChR2) by injecting Cre-inducible recombinant adeno-associated virus (rAAV) expressing ChR2 into the DS of the Cre mouse for spike recording and optogenetic activation. As PV cells usually displayed high-frequency firing, they were targeted with engineered ChR variant ChETA, which could be used to elicit ultra-fast firing frequencies (up to 200 Hz) in fast-spiking cells (Tye and Deisseroth, 2012). SOM-Cre, ChAT-Cre, and PV-Cre mice were used for cell-type-specific expression of fluorescent proteins and photoactivated opsins (ChR2 or ChETA). Drd1a-Cre and Drd2-Cre mice, respectively, were used to express fluorescent proteins and ChR2 in D1 receptor (D1R)-expressing medium spiny neurons (dMSNs) and iMSNs (Barbera et al., 2016; Klaus et al., 2017; Kravitz et al., 2010).

To isolate activity specifically from these cell types, we used a cell-type-specific ("opto-tag") recording method (Figures 2A–2C; for references, see Cohen et al., 2012; Lee et al., 2021; Lima et al., 2009). Recordings were made in freely moving mice by implanting optrodes consisting of 32-channel movable tetrodes coupled to an optic fiber placed just above the DS (Figure S2C; Anikeeva et al., 2011; Xu et al., 2015). Laser pulse trains (10 or 40 Hz, 10 ms per pulse) were applied constantly for 1 min (Figure 2A). Single-unit recording data exhibiting reliable laser-evoked spiking at short latencies were obtained (Figure 2B). To determine whether the observed neuronal activities were optically driven, we set up two criteria (Wolff et al., 2014; Xu et al., 2015): First, neuronal response to laser pulse should occur within a time window of 5 ms; second, the correlation coefficient (CR) between optogenetic induced waveforms and natural spontaneous waveforms must be >0.95 (Figure 2C). After the targeted optically driven waveforms were isolated from all of our mouse lines (Figure 2D), we performed comprehensive waveform feature extraction analysis. Then, different waveform parameters from all of these recorded neurons were plotted (Figure S3).

The plot of interneurons showed that they form distinct clusters. Notably, iMSNs and dMSNs formed two distinctive clusters. dMSNs displayed a shorter positive second phase, while iMSNs displayed waveforms containing a shorter initial positive phase. To further classify these feature profiles, we used principal-component analysis (PCA) followed by unsupervised clustering (Cohen et al., 2012). PCA transforms the raw dataset into a new coordinate system such that the explained variance is maximized on each axis. The plotting yielded distinct clusters in a new coordinate system (Figures 2E and 2F). Notably, the spike waveform of each cell type matched very well with those obtained *in vitro* (Kawaguchi, 1993; Mallet et al., 2005; Wilson et al., 1990) or *in vivo* (Sharott et al., 2009; Wolff et al., 2014), thus validating that the experimental scheme we used is sufficient to distinguish these cell types. Because the waveform of spontaneous and optogenetically induced spiking match very well (CR > 0.95; Figure 2C), in the following experiments, we differentiated putative cell types based on the characteristic waveform features of spontaneous spiking without the opto-tagging procedure (Cohen et al., 2012; Xu et al., 2015).

We next examined the possible changes in the firing rate of these neuron types during the photoinhibition of SNc-DS terminals (Figures 2G–2K). Increased firing rate was observed in ChATs and iMSNs (Figures 2H and 2I). In contrast, firings of the SOMs and dMSNs were reduced (Figures 2G and 2J), consistent with a recent finding in PD mice (Parker et al., 2018). No activity change was observed in identified PV neurons (Figure 2K).

To further examine the exact role that down- or upregulation of distinct interneuron populations play in the downstream DS

CellPress
OPEN ACCESS

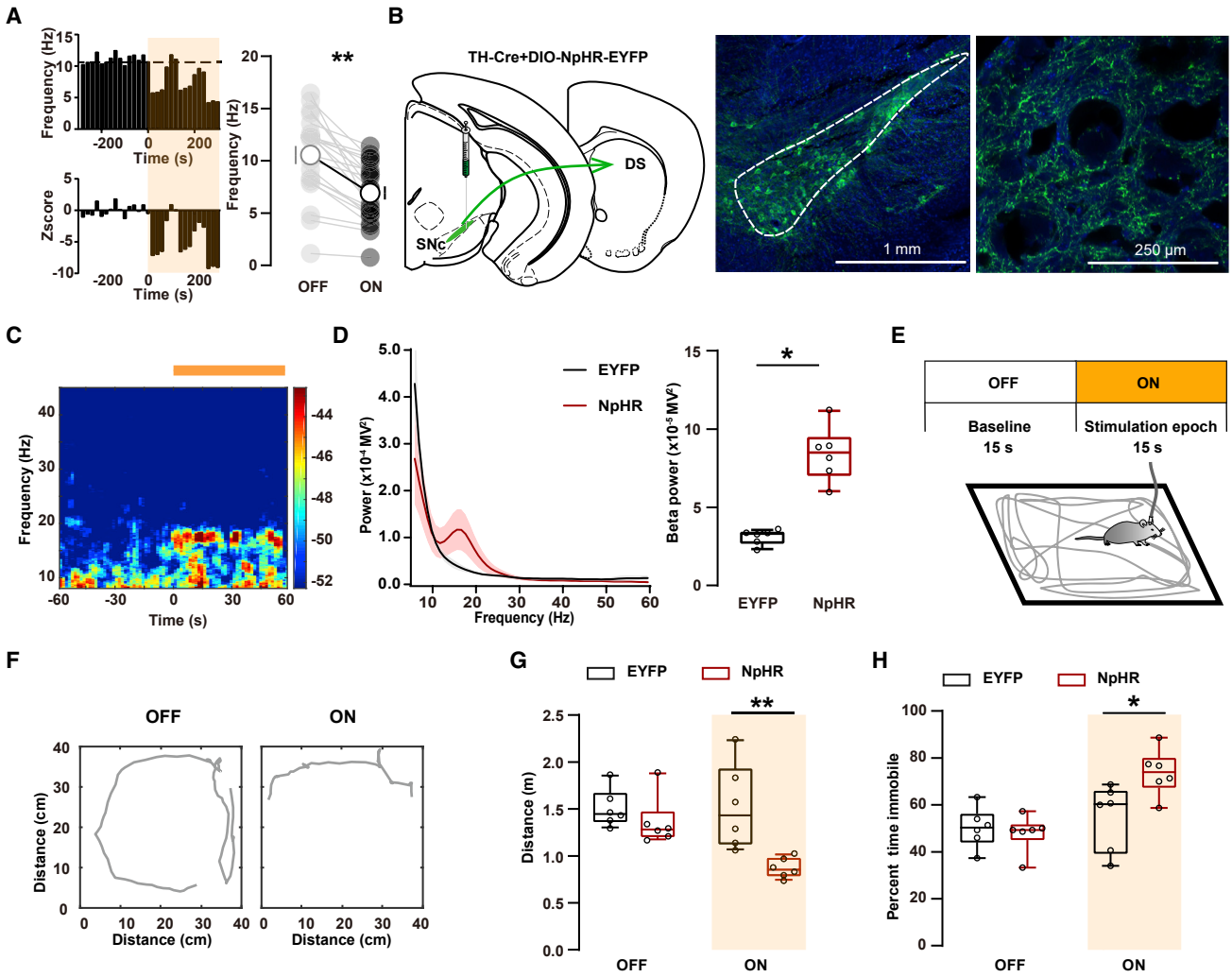

Figure 1. Acute inhibition of dopaminergic control over striatum generates beta oscillations and produces motor deficits

(A) Activity changes in DANs during photoinhibition of SNc DANs (6 mice; DANs: n = 21, Wilcoxon matched-pairs signed rank test, $p < 0.01$).

(B) Schematic showing SNc-to-DS projection (left). Wild-type (WT) mice were injected with TH-Cre and EF1α-DIO-NpHR-EYFP in the SNc (center), and projection fibers in DS were visualized (right).

(C) Representative spectrogram of LFP recorded within a 1-min OFF and 1-min ON duration. Increased beta power was observed upon SNc-DS inhibition. Yellow bar above the spectrogram displays the duration of photoinhibition.

(D) Enhanced beta power during SNc-DS inhibition. (Left) Averaged power spectra of DS LFP. (Right) Statistical plotting showing enhanced beta power (n = 6; unpaired t test; $p < 0.05$).

(E) Open field setup and stimulation protocol.

(F) Example locomotor trajectories before and during laser illumination.

(G and H) Histograms show significant difference in distance traveled (G: n = 6; unpaired t test; $p < 0.01$) and percent time immobile (H: n = 6; unpaired t test; $p < 0.05$) between control and DANs suppression group. Data presented as means ± SEMs. *$p < 0.05$, **$p < 0.01$.

See also Figures S1 and S2.

microcircuits, we took advantage of the principle that monosynaptic connections are associated with precisely timed spiking relationships at short (<5 ms) latency offsets between two connected neurons (Senzai and Buzsáki, 2017). This is usually achieved by examining counts of co-occurrences of spiking in the putative pre- and post-synaptic neurons at various latencies (Fujisawa et al., 2008), as exemplified by the cross-correlation histogram (CCG). These results yielded time sequences for firing alterations in different cell types—in other words, SOMs precede ChATs, iMSNs and dMSNs (Figure 2L). When considering the existence of direct anatomical connections between SOMs and ChATs and dMSNs and iMSNs, these findings suggest that SOMs may function as an upstream regulator for the generation of excessive beta oscillations.

SOM inhibition mimics the effect of SNc DAN inhibition

We next examined the potential contribution of SOMs on the generation of excessive beta oscillations. For this purpose, we

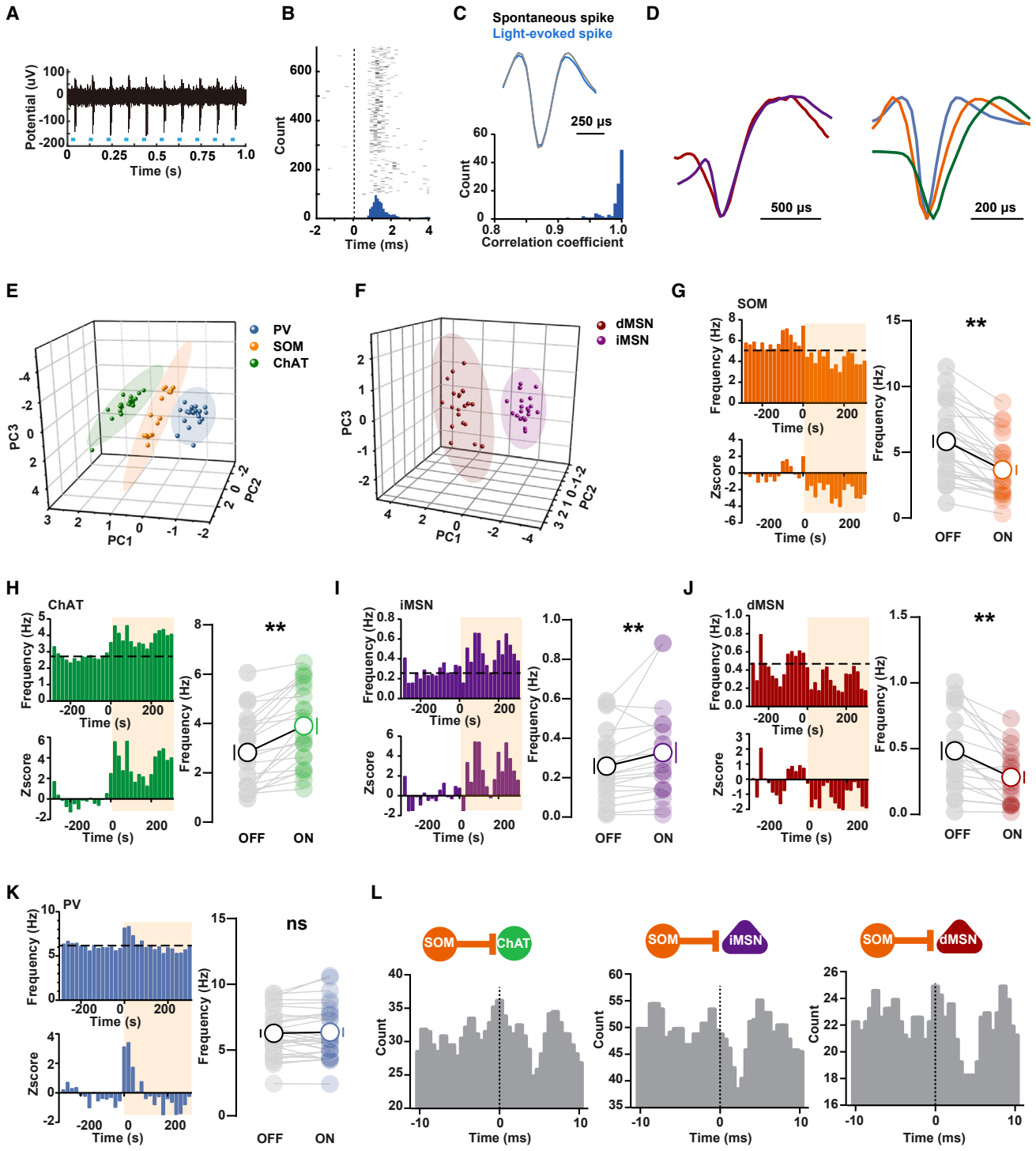

Figure 2. Photoinhibition of SNc-DS projections induced distinct changes in striatal neuron activity

(A) Representative recording of laser-evoked spiking in a ChR2-tagged neuron. Blue lines refer to laser pulses (10 ms, 10 Hz).

(B) Raster plot and peristimulus time histogram (PSTH, bin size, 0.1 ms) for laser-evoked spikes of a sample ChR2-tagged neuron. Dashed line marks the laser onset time.

(C) Waveform comparison between spontaneous and laser-evoked spikes. (Top) Overlaid averaged waveforms of spontaneous spikes (gray) and laser-evoked spikes (blue) of a sample neuron. (Bottom) Distribution of CR between spontaneous spike and laser-evoked spike for all striatal neurons that were optogenetically identified.

(D) Overlaid traces display the distinct waveforms from different types of striatal neurons.

(legend continued on next page)

targeted SOMs with NpHR by injecting Cre-inducible rAAV expressing NpHR into the DS of the SOM-Cre mice (Figures 3A and S2D). Directly deactivated SOMs significantly elevated the power of the beta oscillations (Figures 3B–3D) and excited both ChATs and iMSNs and suppressed dMSNs (Figures 3E–3G). No activity change in PVs was detected (Figure 3H). In a separate set of experiments, we found that deactivation of SOMs significantly reduced the total distance traveled (Figures 3I and 3J) and increased immobility (Figure 3K). Taken together, these data point to the conclusion that SOMs inhibition mimics the effect of SNc DANs inhibition on striatal neuron activity and movement.

iMSNs and ChATs are implicated in the generation of beta oscillations and movement disorder

To examine potential involvements of MSNs and ChATs in the generation of excessive beta oscillations, we simultaneously recorded single-unit firing and LFPs in the DS of freely behaving mice. We calculated spike-field coherence (SFC), a measure of phase synchronization of unit spikes to LFP (Rutishauser et al., 2010; Yang et al., 2018). In mice subjected to SNc-DS photoinhibition, a large fraction of recorded ChATs (n = 13 of 19) and iMSNs (n = 15 of 22) displayed significantly enhanced SFC in the beta band activity with no significant change of SFC in dMSNs (Figures 4A–4C). Photoinhibition of SOMs yielded similar effects on phase synchronization between unit spikes and LFPs (Figures S4A–S4C).

To further assess how single-unit activity was synchronized with beta oscillations, we collected the LFP phase angles that corresponded to the spike times for all of the activations within a time window across all trials (Figures 4D–4F). These neurons were considered significantly phase locked when the distribution of spike phase angles departed from a uniform circular distribution (Hawking and Gerdjikov, 2013). Before illumination (control group), ChATs, iMSNs, and dMSNs spiking occurs at all phases of beta oscillations (left in each panel). Accordingly, these cells in the control group exhibited a weak tendency to fire around the troughs of the beta oscillations, indicating the absence of phase-locked firings. In contrast, a substantial proportion of the identified ChATs and iMSNs showed a significant tendency to phase-lock their firing to ongoing beta oscillations during SNc-DS (17 of 22 ChATs; 22 of 28 iMSNs) or SOMs inhibition (14 of 19 ChATs; 16 of 21 iMSNs; right in each panel). The phase angles between ChATs spiking and LFP beta oscillations were significantly clustered around 180°–270° (n = 17 cells, 4 mice), whereas the phase angles of iMSNs clustered around 270°–360° (n = 22 cells, 4 mice). dMSNs fired at all phases of beta oscillations both OFF and ON stage, indicating that the timing of dMSNs firing (phase of the vectors) was relatively more uniformly distributed and thus as a population did not phase lock at specific phases of beta oscillations. Similar observations were obtained when photoinhibitions were exerted directly on SOMs instead of on SNc-DS projections (Figures S4D–S4F).

The high correlation of both ChATs and iMSNs activities with enhanced beta power suggests that they may be implicated in the generation of beta oscillations. Based on the reciprocal anatomical projections and putative synaptic connection between ChATs and iMSNs (Figures S5A and S5I; for references, see Deffains and Bergman, 2015; Steiner and Tseng, 2017), we hypothesized that they may constitute a loop-like circuitry motif that underlies the generation of excessive beta oscillations in DS. To test this possibility, we activated ChATs in DS with either transient (20 Hz, 2 min; Figure S5) or constant (2 min; Figure S6) mild illumination to see whether this could promote the generation of beta oscillations. Our results indicate that the transient activation of ChATs or iMSNs promotes beta oscillation generation and produces motor deficits. These results also point to the notion that a loop microcircuit constituted by ChATs and iMSNs may function as a downstream effector of SNc DANs or SOMs for the generation of beta oscillations in DS.

Closed-loop inhibition targeting iMSNs or ChATs suppresses beta oscillations and ameliorates motor deficits

To confirm the role of ChAT-iMSN loop in beta oscillation generation, we used closed-loop optogenetic interventions based on real-time detection of beta oscillations in DS (Figure 5A). The principle is that once the enhancement in LFP beta power in DS was detected above 3-fold standard deviation (SD), light was delivered immediately (delay <40 ms) through laser fiber to deliver optogenetic inhibition selectively on iMSNs. Then, the overall effect on beta oscillations would be evaluated. To achieve this experimental design, we stereotactically implanted the laser fiber into SNc for DAN photoinhibition and implanted the optrode into DS for both optogenetic manipulation and LFP recording (Figure S2H). Mixed high-titer viruses (TH-Cre and EF1α-DIO-NpHR-mCherry) were injected into lateral SNc at the right side to selectively express NpHR in DANs. EF1α-DIO-SwiChRca-EYFP were injected into DS of Drd2-Cre mice to selectively express SwiChRca in iMSNs in DS. SwiChRca is a class of ChRs (originally cation conducting) that is converted into chloride-conducting anion channels (Berndt et al., 2014). The original blue light-activation spectrum of C1C2 (a chimera between ChR1 and ChR2 from *Chlamydomonas reinhardtii*) is maintained. This enables SwiChRca-expressing iMSNs to be inhibited by 473 nm light and to avoid the overlap of spectral wavelength between the opto-inhibition of NpHR-expressing DANs (593 nm) and SwiChRca-expressing iMSNs in the striatum.

In vivo multi-channel LFP recordings were performed at DS in freely behaving mice. Briefly, the wide-band signal was band-pass filtered (12–25 Hz). The filtered LFPs were then rectified

(E and F) Separation of striatal neuron subtypes based on PCA for optogenetically identified interneurons (E) or MSNs (F).
(G–K) Activity changes in optogenetically identified neurons during photoinhibition of SNc-DS projections (dashed line: average baseline firing, 6 mice; SOMs: n = 30, Wilcoxon matched-pairs signed rank test, $p < 0.01$; ChATs: n = 22, paired t test, $p < 0.01$; iMSNs: n = 24, Wilcoxon matched-pairs signed rank test, $p < 0.01$; dMSNs: n = 28, Wilcoxon matched-pairs signed rank test, $p < 0.01$; PVs: n = 30, paired t test, $p > 0.05$).
(L) Examples of CCG between neuron pairs reveal putative synaptic connections among different neuron subtypes. Data presented as means ± SEMs. $^{**}p < 0.01$, ns, no significance.
See also Figures S2 and S3.

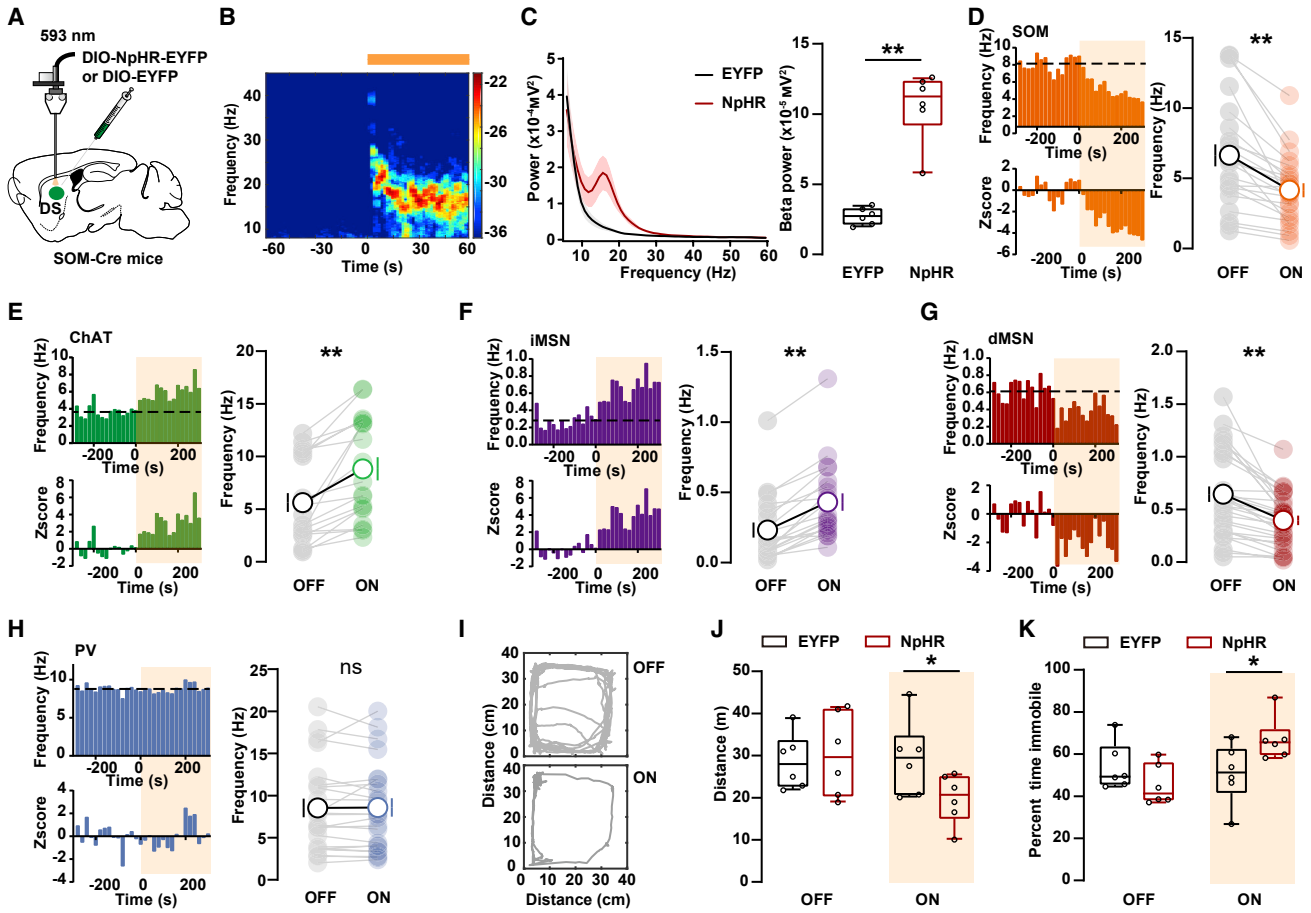

Figure 3. SOM inhibition mimics the effect of SNc DAN inhibition on striatal neuron activity and locomotion

(A) Localization of viral injection and recording.

(B) Representative spectrogram of LFP data recorded from DS. Increased beta power was observed upon SOM inhibition.

(C) Enhanced beta power during SOM inhibition. (Left) Averaged power spectra of DS LFP. (Right) Statistical plotting showing enhanced beta power during photoinhibition of SOMs (n = 6; Mann-Whitney test, $p < 0.01$).

(D–H) Activity changes in striatal neuron subtypes during photoinhibition of SOMs. Significant elevations in ChAT and iMSN firing rates were observed (6 mice; Wilcoxon matched-pairs signed rank test; ChAT neuron: n = 19, $p < 0.01$; iMSN neuron: n = 24, $p < 0.01$). In contrast, firing of SOM and dMSN neurons decreased (6 mice; paired t test; SOMs: n = 23; $p < 0.01$; dMSNs: n = 28, $p < 0.01$). No activity change in PV was detected (6 mice; PVs: n = 23, Wilcoxon matched-pairs signed rank test, $p > 0.05$).

(I) Examples of the effect of SOM photoinhibition on mice movement trajectory.

(J and K) Histograms show significant difference in distance traveled (n = 6; unpaired t test; $p < 0.05$) and percent time immobile (n = 6; unpaired t test; $p < 0.05$) between control and SOM suppression groups. Data presented as means ± SEMs. *$p < 0.05$, **$p < 0.01$, ns, no significance.

See also Figure S2.

and smoothed using a moving average filter of 400-ms duration to generate an online value of beta amplitude (Little et al., 2013). As shown in Figure 5B, beta oscillations were generated by photoinhibiting virus-infected DANs in SNc. A custom-designed detection algorithm processed by MATLAB was used to detect the enhancement of beta power in real time, which was also used to trigger the online optogenetic manipulation (473 nm) with a delay <40 ms (see STAR Methods for more details). Closed-loop photoinhibition of iMSNs triggered by LFP beta power increments (>3 SD) largely suppressed the excessive beta power compared to that before intervention (Figures 5C–5E). As a control, the delivery of randomized stimulation was not based on the increment of beta power. Although the total stimulation duration was the same as closed-loop intervention, the randomized intervention failed to exhibit any influence on beta power. Thus, the successful closed-loop intervention of beta oscillations via the selective photoinhibition of iMSNs helps to establish a causal link between iMSNs activation and generation of beta oscillations.

Given the correlation of beta oscillations and movement disorders, we next investigated whether suppression of beta oscillations with this closed-loop intervention alleviated the deficit in motor function. In an open field, we evaluated the spontaneous locomotion of mice by calculating the total distance traveled and percent time of immobility during period of baseline, DANs photoinhibition, DANs photoinhibition plus closed-loop

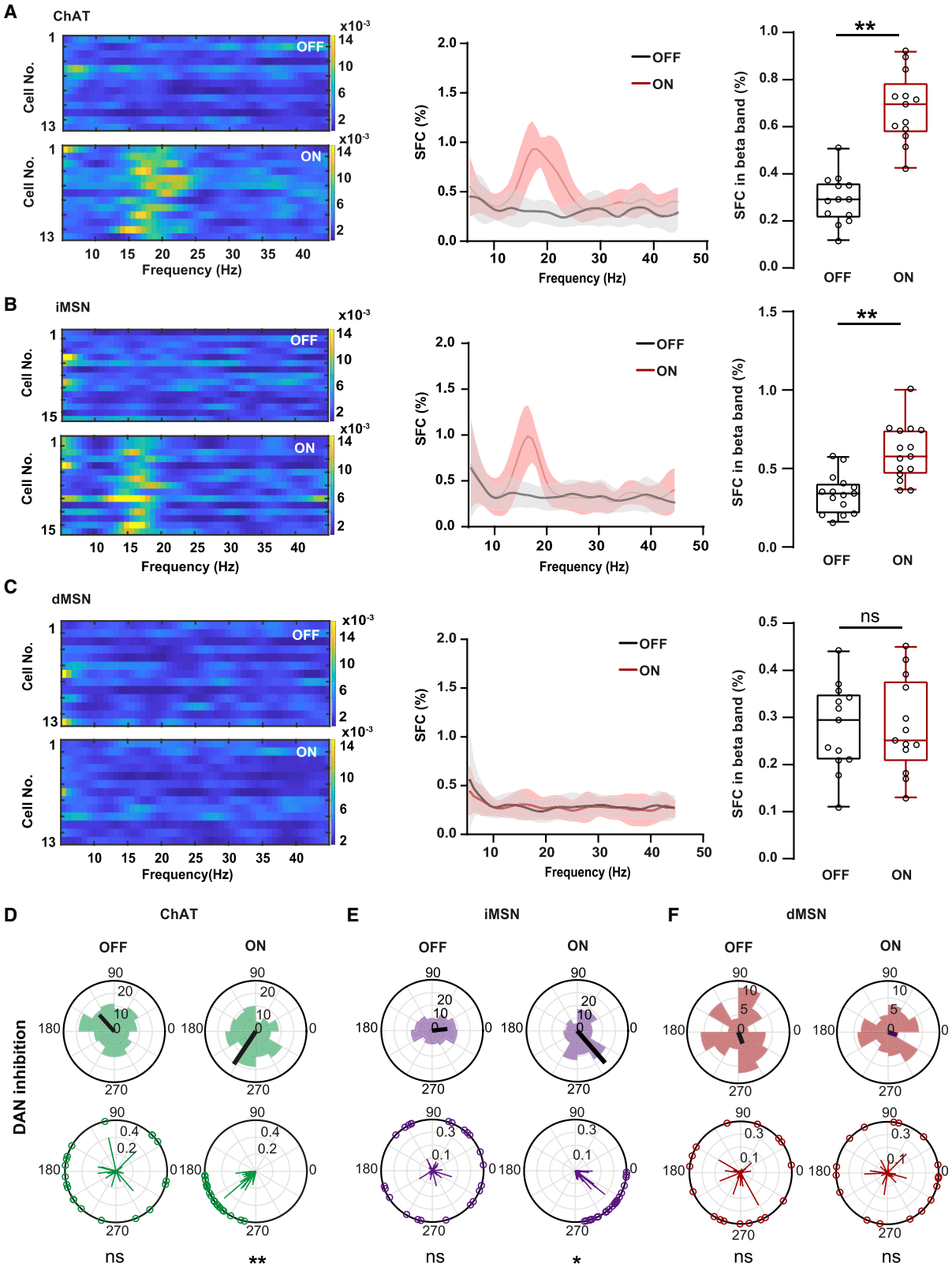

(legend on next page)

intervention, and DANs photoinhibition plus random intervention. The impaired locomotion during photoinhibition of DANs in SNc was completely restored during the closed-loop optogenetic intervention of beta oscillation (Figures 5F and 5G). As a control, no such improvement in motor function was observed during randomized optogenetic intervention. Similar observations were obtained when closed-loop inhibition targeted ChATs (Figures 5H–5K and S2H). These results indicate that closed-loop inhibition targeting iMSNs or ChATs suppresses beta oscillations and ameliorates motor deficits.

DISCUSSION

Striatum can be the origin of beta oscillation generation

The potential for striatum as the origin of beta oscillations has been previously ignored, largely due to the fact that the inhibitory striatal network cannot easily generate any rhythmic activity at a relatively high frequency. This concept was updated by recent studies on both modeling and *in vivo* experiments (McCarthy et al., 2011; Kondabolu et al., 2016; Bar-Gad et al., 2004; Tachibana et al., 2011). However, there have been two other theories that speculated on the origin of excessive beta oscillations. Evidence for the globus pallidus externa-subthalamic nucleus (GPe-STN) pacemaker hypothesis comes from a study showing that GPe-STN loop was able to generate synchronized oscillatory bursting activity *in vitro* (Plenz and Kital, 1999). However, the relatively low rate of frequency (0.4–1.8 Hz) means that the bursting activity is more likely an amplifier or maintainer of external oscillatory activity at the beta band. The oscillations at the beta band recorded in the GPe-STN loop would more likely stem from external inputs. Notably, striatum is such an upstream region that sends direct projection to GPe. Another theory proposed that cortical patterning of the STN engenders beta generation in PD (Bevan et al., 2002). A complete map for the origin of the excessive beta oscillations in PD has not yet been established. We demonstrate here that the reduced activity of DANs may lead to abnormal beta frequency within the striatum. Notably, these data do not invalidate the notion that the GPe-STN network is critical for parkinsonian beta oscillations, but rather, propose an alternative view that the circuitry mechanism we demonstrated is complementary to the GPe-STN resonance.

Acute deactivation of SNc DANs produces beta oscillations in striatum

Although DANs degeneration is a chronic process in PD, beta oscillations can be elevated rapidly in the striatum by acute reduction of dopamine, accompanied by PD-like hypokinesia and akinesia (Costa et al., 2006). An elegant study reported that optogenetic activation of striatal ChATs with a Poisson-distributed 40-Hz laser light pulse train robustly increased oscillations in the striatum across broad frequencies, including frequency at the beta band (Kondabolu et al., 2016). We found that the inhibition of SNc DANs only decreased the firing frequency of DANs from 10.55 to 6.93 Hz. This may be due to partial infection of DANs with rAAV. Direct optogenetic inhibition of SNc dopaminergic terminals in the striatum can rapidly produce beta oscillations with a frequency (12–25 Hz) similar to that observed in other studies (Costa et al., 2006; McCarthy et al., 2011). Furthermore, this effect can be mimicked by the optogenetic inhibition of SOMs or by the activation of either ChATs or iMSNs. Our results showed at a cell-type-specific level the repercussions of DA neuron silencing on the generation of beta oscillations and concomitant local intrastriatal striatal networks involving iMSNs, ChAT, and SOM cells. However, as our study was performed on normal animals, we should take note of the possible involvement of chronic changes in neural circuits for beta oscillation generations in PD.

A SOM-driven ChAT-iMSN loop for beta oscillation generation in striatum

An exciting finding is the distinct spike waveforms in D1-and D2-expression MSNs. Striatal MSNs have long been thought to be homogeneous in their somatodendritic morphology and physiology, but this concept was challenged by studies (Al-Muhtasib et al., 2018; Bergonzoni et al., 2021; Gertler et al., 2008). By using Drd1a-Cre and Drd2-Cre mice, we could distinguish and monitor firing activities in dMSNs and iMSNs in the striatum. The first reported distinct waveforms of iMSNs and dMSNs enable us to examine potential activity changes of the two cell populations separately.

We proposed that the ChAT-iMSN loop is the circuit motif that could be driven by SOMs and contributes to the generation of beta oscillations. Several pieces of evidence in the present study support this hypothesis. First, the spike firings of both ChAT and iMSN cells are temporally correlated with and phase locked to LFP at beta oscillations. Second, directly activating either striatal ChATs or iMSNs can mutually promote the power of beta oscillations and the phase locking between spike firings and LFP. Third, closed-loop inhibition targeting iMSNs or ChATs suppresses beta oscillations.

Limitations of the study

Our findings suggest that the CBT network components that modulate beta oscillations in normal states may be operational

Figure 4. Activity changes in ChATs and iMSNs are implicated in the generation of beta oscillations

(A–C) SFC of neurons recorded from the ChATs, iMSNs, and dMSNs. (Left) SFC of each unit; (center) average SFC; (right) percent SFC in beta band (ChATs: $n = 13$, $p < 0.01$; iMSNs: $n = 15$, $p < 0.01$; dMSNs: $n = 13$, $p > 0.05$; paired t test).

(D–F) Polar plots indicating the distribution of LFP beta oscillation phase angles at which spikes occur for the example neurons (top panel) and the phase angles for all of the neurons in the population (bottom panel). The black lines are resultant phase vectors obtained by vector averaging the phase of the spikes for the unit illustrated, where the line length represents the resultant magnitude; each radius in the lower plots represents the resultant vector of one unit. The numbers in the top plots are raw spike counts and the numbers in the lower plots are the magnitudes of the resultant vectors based on each spike having magnitude 1. OFF and ON refer to before and during SNc-DS photoinhibition, respectively. During DAN inhibition (ON stage), ChATs and iMSNs were, respectively, clustered around 180°–270° and 270°–360° (Rayleigh's test for circular uniformity; ChATs: $n = 17$, OFF, $p > 0.05$, ON, $p < 0.01$; iMSNs: $n = 22$, OFF, $p > 0.05$, ON, $p < 0.05$; dMSNs: $n = 17$, OFF, $p > 0.05$, ON, $p > 0.05$). Data presented as means ± SEMs. *$p < 0.05$, **$p < 0.01$, ns, no significance.

See also Figures S4–S6.

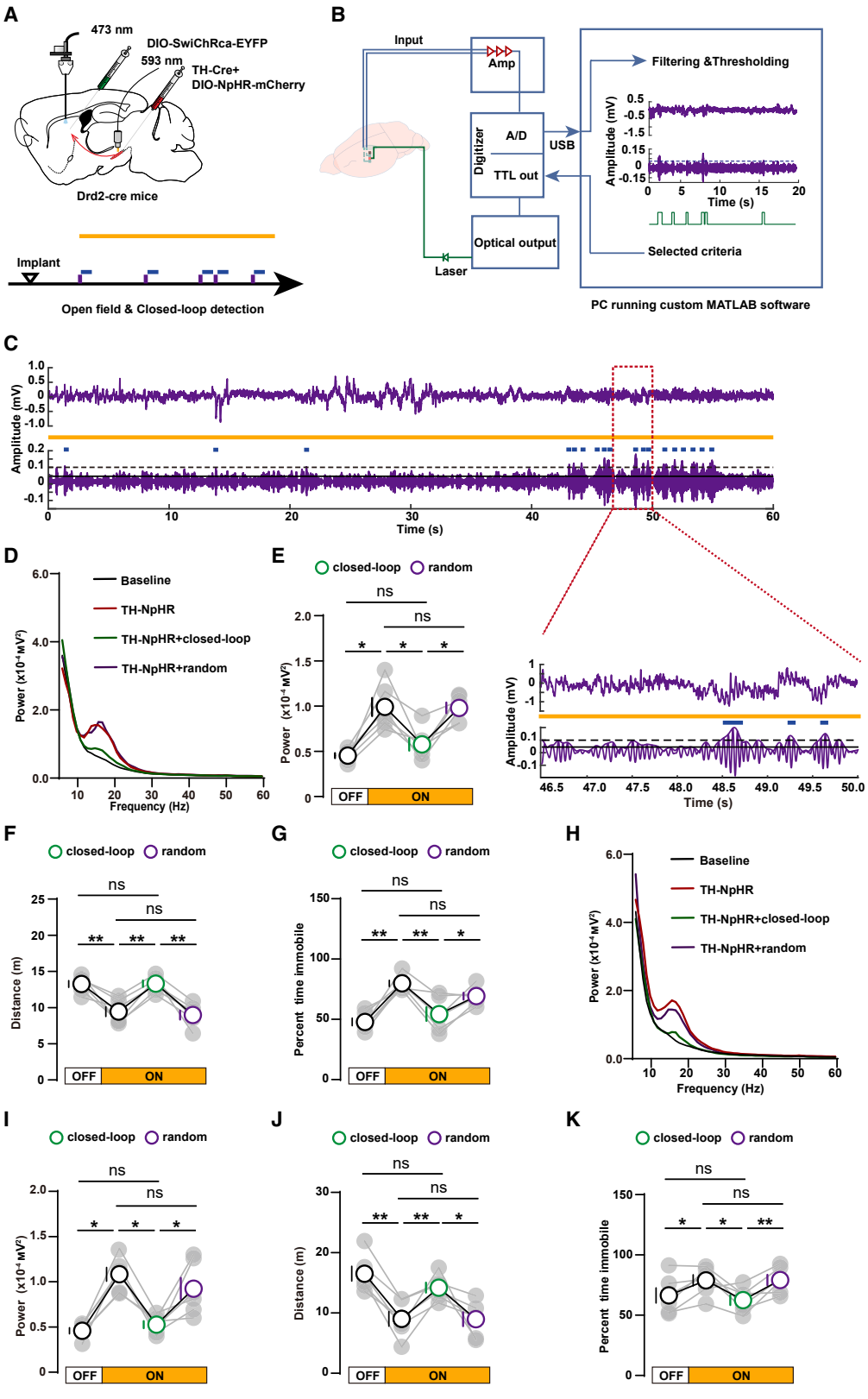

(legend on next page)

in PD states. In particular, optogenetic operation of a striatal SOM-driven ChAT-iMSN loop alone, which enable us easily manipulate DA release and downstream operators, can generate both beta oscillations and motor deficits. Nevertheless, the multiple plastic changes seen throughout the CBT loop due to the chronic loss of dopamine may not be present in our current experiments, and we do not consider the acute DA neurons inhibition state equivalent to the parkinsonian state. In the present study, the recording and behavioral measures of beta oscillations were not performed simultaneously; thus, the relevance of beta oscillations to the motor deficits still required further evidence. Moreover, we should not totally exclude the possible involvement of chronic plastic changes in other CBT network components, such as the GPe-STN loop, in the generation of beta oscillations. Therefore, our present findings may be considered an important complement to former investigations in chronic parkinsonian models.

STAR★METHODS

Detailed methods are provided in the online version of this paper and include the following:

- KEY RESOURCES TABLE
- RESOURCE AVAILABILITY
  - Lead contact
  - Materials availability
  - Data and code availability
- EXPERIMENTAL MODEL AND SUBJECT DETAILS
- METHOD DETAILS
  - Virus preparation
  - Surgical procedures
  - Optogenetic manipulation
  - Optrode recordings and optogenetic identification of striatal neurons
  - Spike sorting
  - Data analysis
  - Behavioral assays
  - Anatomical verification
  - Immunofluorescence
  - Closed-loop optogenetic intervention
- QUANTIFICATION AND STATISTICAL ANALYSIS

SUPPLEMENTAL INFORMATION

Supplemental information can be found online at https://doi.org/10.1016/j.celrep.2022.111111.

ACKNOWLEDGMENTS

We thank Dr. Minmin Luo, Shengxi Wu, Fuqiang Xu, and Peng Cao for kindly providing Drd1-Cre, Drd2-Cre, SOM-IRES-Cre, ChAT-IRES-Cre, and PV-IRES-Cre mice. This research was supported by grants to W.L. from the National Natural Science Foundation of China (31730107) and the Ministry of Science and Technology (2021ZD0203502), grants to D.Z. from Science and Technology Innovation 2030 (2021ZD0200204), the National Natural Science Foundation of China (12071287), the Shanghai Municipal Science and Technology Major Project 2021SHZDZX0102, and the Student Innovation Center at Shanghai Jiao Tong University, and grants to S.W. from the China Postdoctoral Science Foundation (2019M651659). We thank all members of the Lu and Zhou labs for discussion and support. We also thank Ms. He Yang for help on editing the manuscript.

AUTHOR CONTRIBUTIONS

Conceptualization, D.Q., J.X., and W.L.; methodology, Y.W., Z.W., T.S., and S.L.; software, Y.W. and Q.W.; formal analysis, D.Q., W.L., J.X., J.Y., and S.Q.; investigation, D.Q., W.L., and J.X.; writing – original draft, W.L. and D.Z.; writing – review & editing, W.L. and D.Z.; supervision, W.L., D.Z., Q.W., Y.S., L.C., and T.-F.Y.; funding acquisition, W.L., D.Z., and S.W.

DECLARATION OF INTERESTS

The authors declare no competing interests.

Received: December 5, 2021
Revised: April 24, 2022
Accepted: June 28, 2022
Published: July 19, 2022

REFERENCES

Al-Muhtasib, N., Forcelli, P.A., and Vicini, S. (2018). Differential electrophysiological properties of D1 and D2 spiny projection neurons in the mouse nucleus accumbens core. Physiol. Rep. *6*, e13784.

Anikeeva, P., Andalman, A.S., Witten, I., Warden, M., Goshen, I., Grosenick, L., Gunaydin, L.A., Frank, L.M., and Deisseroth, K. (2011). Optetrode: a

Figure 5. Closed-loop inhibition targeting iMSNs or ChATs suppresses beta oscillations and ameliorates motor deficits

(A) Localization of viral injections, optrode and fiber-optic implantation (top), and timeline for successive photoinhibitions of SNc DANs (bottom, yellow bar) and iMSNs (blue bars).

(B) Experimental setup for closed-loop photoinhibition.

(C) Sample section of closed-loop intervention and recordings. (Top) Raw LFP. (Bottom) Band-pass filtered LFP. The period marked by dotted line box was magnified and displayed below.

(D) Averaged power spectra of DS LFP from different treated groups.

(E) Closed-loop inhibition of iMSNs suppressed LFP beta power. As a control, randomized inhibition of iMSNs failed to display similar effect on beta oscillations. The bar labeled OFF and ON at the bottom of each plot refers to before and during DANs photoinhibition. The gray symbols represent data of individual animals (n = 6; Wilcoxon matched-pairs signed rank test).

(F) Line chart shows comparison of total distance in different treated groups (n = 6, paired t test).

(G) Line chart shows comparison of percent time immobile in different treated groups (n = 6; paired t test).

(H–K) Data presented as in (D)–(G) for closed-loop inhibition of ChATs.

(I) Closed-loop inhibition of ChATs suppressed LFP beta power (n = 6; Wilcoxon matched-pairs signed rank test).

(J) Line chart shows comparison of total distance in different treated groups (n = 6; paired t test).

(K) Line chart shows comparison of percent time immobile in different treated groups (n = 6; paired t test). Data presented as means ± SEMs. *$p < 0.05$, **$p < 0.01$; ns, no significance.

See also Figure S2.

multichannel readout for optogenetic control in freely moving mice. Nat. Neurosci. *15*, 163–170. https://doi.org/10.1038/nn.2992.

Barbera, G., Liang, B., Zhang, L., Gerfen, C., Culurciello, E., Chen, R., Li, Y., and Lin, D.T. (2016). Spatially compact neural clusters in the dorsal striatum encode locomotion relevant information. Neuron *92*, 202–213. https://doi.org/10.1016/j.neuron.2016.08.037.

Bar-Gad, I., Elias, S., Vaadia, E., and Bergman, H. (2004). Complex locking rather than complete cessation of neuronal activity in the globus pallidus of a 1-methyl-4-phenyl-1, 2, 3, 6-tetrahydropyridine-treated primate in response to pallidal microstimulation. J. Neurosci. *24*, 7410–7419. https://doi.org/10.1523/jneurosci.1691-04.2004.

Bergonzoni, G., Döring, J., and Biagioli, M. (2021). D1R- and D2R-medium-sized spiny neurons diversity: insights into striatal vulnerability to Huntington's disease mutation. Front. Cell. Neurosci. *15*, 628010. https://doi.org/10.3389/fncel.2021.628010.

Berke, J.D. (2008). Uncoordinated firing rate changes of striatal fast-spiking interneurons during behavioral task performance. J. Neurosci. *28*, 10075–10080. https://doi.org/10.1523/jneurosci.2192-08.2008.

Berndt, A., Lee, S.Y., Ramakrishnan, C., and Deisseroth, K. (2014). Structure-guided transformation of channelrhodopsin into a light-activated chloride channel. Science *344*, 420–424. https://doi.org/10.1126/science.1252367.

Bevan, M., Magill, P.J., Terman, D., Bolam, J.P., and Wilson, C.J. (2002). Move to the rhythm: oscillations in the subthalamic nucleus-external globus pallidus network. Trends Neurosci. *25*, 525–531. https://doi.org/10.1016/s0166-2236(02)02235-x.

Bokil, H., Andrews, P., Kulkarni, J.E., Mehta, S., and Mitra, P.P. (2010). Chronux: a platform for analyzing neural signals. J. Neurosci. Methods *192*, 146–151. https://doi.org/10.1016/j.jneumeth.2010.06.020.

Brazhnik, E., McCoy, A.J., Novikov, N., Hatch, C.E., and Walters, J.R. (2016). Ventral medial thalamic nucleus promotes synchronization of increased high beta oscillatory activity in the basal ganglia-thalamocortical network of the Hemiparkinsonian rat. J. Neurosci. *36*, 4196–4208. https://doi.org/10.1523/jneurosci.3582-15.2016.

Brown, P. (2007). Abnormal oscillatory synchronisation in the motor system leads to impaired movement. Curr. Opin. Neurobiol. *17*, 656–664. https://doi.org/10.1016/j.conb.2007.12.001.

Chuhma, N., Tanaka, K.F., Hen, R., and Rayport, S. (2011). Functional connectome of the striatal medium spiny neuron. J. Neurosci. *31*, 1183–1192. https://doi.org/10.1523/jneurosci.3833-10.2011.

Cohen, J.Y., Haesler, S., Vong, L., Lowell, B.B., and Uchida, N. (2012). Neuron-type-specific signals for reward and punishment in the ventral tegmental area. Nature *482*, 85–88. https://doi.org/10.1038/nature10754.

Costa, R.M., Lin, S.C., Sotnikova, T., Cyr, M., Gainetdinov, R., Caron, M., and Nicolelis, M. (2006). Rapid alterations in corticostriatal ensemble coordination during acute dopamine-dependent motor dysfunction. Neuron *52*, 359–369. https://doi.org/10.1016/j.neuron.2006.07.030.

Deffains, M., and Bergman, H. (2015). Striatal cholinergic interneurons and cortico-striatal synaptic plasticity in health and disease. Mov. Disord. *30*, 1014–1025. https://doi.org/10.1002/mds.26300.

Dogbevia, G.K., Roβmanith, M., Sprengel, R., and Hasan, M.T. (2016). Flexible, AAV-equipped genetic modules for inducible control of gene expression in mammalian brain. Mol. Ther. Nucleic Acids *5*, e309. https://doi.org/10.1038/mtna.2016.23.

Fujisawa, S., Amarasingham, A., Harrison, M.T., and Buzsáki, G. (2008). Behavior-dependent short-term assembly dynamics in the medial prefrontal cortex. Nat. Neurosci. *11*, 823–833. https://doi.org/10.1038/nn.2134.

Garas, F.N., Shah, R.S., Kormann, E., Doig, N.M., Vinciati, F., Nakamura, K.C., Dorst, M.C., Smith, Y., Magill, P.J., and Sharott, A. (2016). Secretagogin expression delineates functionally-specialized populations of striatal parvalbumin-containing interneurons. Elife *5*, e16088. https://doi.org/10.7554/elife.16088.

Gertler, T.S., Chan, C.S., and Surmeier, D.J. (2008). Dichotomous anatomical properties of adult striatal medium spiny neurons. J. Neurosci. *28*, 10814–10824. https://doi.org/10.1523/jneurosci.2660-08.2008.

Hawking, T.G., and Gerdjikov, T.V. (2013). Populations of striatal medium spiny neurons encode vibrotactile frequency in rats: modulation by slow wave oscillations. J. Neurophysiol. *109*, 315–320. https://doi.org/10.1152/jn.00489.2012.

Kawaguchi, Y. (1993). Physiological, morphological, and histochemical characterization of three classes of interneurons in rat neostriatum. J. Neurosci. *13*, 4908–4923. https://doi.org/10.1523/jneurosci.13-11-04908.1993.

Klaus, A., Martins, G.J., Paixao, V.B., Zhou, P., Paninski, L., and Costa, R.M. (2017). The spatiotemporal organization of the striatum encodes action space. Neuron *95*, 1171–1180. https://doi.org/10.1016/j.neuron.2017.10.031.

Kondabolu, K., Roberts, E.A., Bucklin, M., McCarthy, M.M., Kopell, N., and Han, X. (2016). Striatal cholinergic interneurons generate beta and gamma oscillations in the corticostriatal circuit and produce motor deficits. Proc. Natl. Acad. Sci. USA *113*, E3159–E3168. https://doi.org/10.1073/pnas.1605658113.

Kravitz, A.V., Freeze, B.S., Parker, P.R.L., Kay, K., Thwin, M.T., Deisseroth, K., and Kreitzer, A.C. (2010). Regulation of parkinsonian motor behaviours by optogenetic control of basal ganglia circuitry. Nature *466*, 622–626. https://doi.org/10.1038/nature09159.

Leblois, A., Meissner, W., Bioulac, B., Gross, C.E., Hansel, D., and Boraud, T. (2007). Late emergence of synchronized oscillatory activity in the pallidum during progressive Parkinsonism. Eur. J. Neurosci. *26*, 1701–1713. https://doi.org/10.1111/j.1460-9568.2007.05777.x.

Lee, J.Y., Jun, H., Soma, S., Nakazono, T., Shiraiwa, K., Dasgupta, A., Nakagawa, T., Xie, J.L., Chavez, J., Romo, R., et al. (2021). Dopamine facilitates associative memory encoding in the entorhinal cortex. Nature *598*, 321–326. https://doi.org/10.1038/s41586-021-03948-8.

Lima, S.Q., Hromádka, T., Znamenskiy, P., and Zador, A.M. (2009). PINP: a new method of tagging neuronal populations for identification during in vivo electrophysiological recording. PLoS One *4*, e6099. https://doi.org/10.1371/journal.pone.0006099.

Little, S., Pogosyan, A., Neal, S., Zavala, B., Zrinzo, L., Hariz, M., Foltynie, T., Limousin, P., Ashkan, K., FitzGerald, J., et al. (2013). Adaptive deep brain stimulation in advanced Parkinson disease. Ann. Neurol. *74*, 449–457. https://doi.org/10.1002/ana.23951.

Mallet, N., Le Moine, C., Charpier, S., and Gonon, F. (2005). Feedforward inhibition of projection neurons by fast-spiking GABA interneurons in the rat striatum in vivo. J. Neurosci. *25*, 3857–3869. https://doi.org/10.1523/jneurosci.5027-04.2005.

Mallet, N., Pogosyan, A., Sharott, A., Csicsvari, J., Bolam, J.P., Brown, P., and Magill, P.J. (2008). Disrupted dopamine transmission and the emergence of exaggerated beta oscillations in subthalamic nucleus and cerebral cortex. J. Neurosci. *28*, 4795–4806. https://doi.org/10.1523/jneurosci.0123-08.2008.

McCarthy, M.M., Moore-Kochlacs, C., Gu, X., Boyden, E.S., Han, X., and Kopell, N. (2011). Striatal origin of the pathologic beta oscillations in Parkinson's disease. Proc. Natl. Acad. Sci. USA *108*, 11620–11625. https://doi.org/10.1073/pnas.1107748108.

Nakamura, K.C., Sharott, A., and Magill, P.J. (2014). Temporal coupling with cortex distinguishes spontaneous neuronal activities in identified basal ganglia-recipient and cerebellar-recipient zones of the motor thalamus. Cereb. Cortex *24*, 81–97. https://doi.org/10.1093/cercor/bhs287.

Parker, J.G., Marshall, J.D., Ahanonu, B., Wu, Y.W., Kim, T.H., Grewe, B.F., Zhang, Y., Li, J.Z., Ding, J.B., Ehlers, M.D., and Schnitzer, M.J. (2018). Diametric neural ensemble dynamics in parkinsonian and dyskinetic states. Nature *557*, 177–182. https://doi.org/10.1038/s41586-018-0090-6.

Plenz, D., and Kital, S.T. (1999). A basal ganglia pacemaker formed by the subthalamic nucleus and external globus pallidus. Nature *400*, 677–682. https://doi.org/10.1038/23281.

Rutishauser, U., Ross, I.B., Mamelak, A.N., and Schuman, E.M. (2010). Human memory strength is predicted by theta-frequency phase-locking of single neurons. Nature *464*, 903–907. https://doi.org/10.1038/nature08860.

Senzai, Y., and Buzsáki, G. (2017). Physiological properties and behavioral correlates of Hippocampal granule cells and mossy cells. Neuron *93*, 691–704.e5. https://doi.org/10.1016/j.neuron.2016.12.011.

Sharott, A., Magill, P.J., Harnack, D., Kupsch, A., Meissner, W., and Brown, P. (2005). Dopamine depletion increases the power and coherence of beta-oscillations in the cerebral cortex and subthalamic nucleus of the awake rat. Eur. J. Neurosci. *21*, 1413–1422. https://doi.org/10.1111/j.1460-9568.2005.03973.x.

Sharott, A., Moll, C.K.E., Engler, G., Denker, M., Grün, S., and Engel, A.K. (2009). Different subtypes of striatal neurons are selectively modulated by cortical oscillations. J. Neurosci. *29*, 4571–4585. https://doi.org/10.1523/jneurosci.5097-08.2009.

Sharott, A., Doig, N.M., Mallet, N., and Magill, P.J. (2012). Relationships between the firing of identified striatal interneurons and spontaneous and driven cortical activities in vivo. J. Neurosci. *32*, 13221–13236. https://doi.org/10.1523/jneurosci.2440-12.2012.

Sharott, A., Vinciati, F., Nakamura, K.C., and Magill, P.J. (2017). A population of indirect pathway striatal projection neurons is selectively entrained to parkinsonian beta oscillations. J. Neurosci. *37*, 9977–9998. https://doi.org/10.1523/jneurosci.0658-17.2017.

Stauffer, W.R., Lak, A., Yang, A., Borel, M., Paulsen, O., Boyden, E.S., and Schultz, W. (2016). Dopamine neuron-specific optogenetic stimulation in rhesus macaques. Cell *166*, 1564–1571.e6. https://doi.org/10.1016/j.cell.2016.08.024.

Steiner, H., and Tseng, K.Y. (2017). Handbook of Basal Ganglia Structure and Function (Elsevier science BV). Chapter 8: GABAergic Interneurons of the Striatum (Bennett, T).

Tachibana, Y., Iwamuro, H., Kita, H., Takada, M., and Nambu, A. (2011). Subthalamo-pallidal interactions underlying parkinsonian neuronal oscillations in the primate basal ganglia. Eur. J. Neurosci. *34*, 1470–1484. https://doi.org/10.1111/j.1460-9568.2011.07865.x.

Tepper, J.M., and Bolam, J.P. (2004). Functional diversity and specificity of neostriatal interneurons. Curr. Opin. Neurobiol. *14*, 685–692. https://doi.org/10.1016/j.conb.2004.10.003.

Tye, K.M., and Deisseroth, K. (2012). Optogenetic investigation of neural circuits underlying brain disease in animal models. Nat. Rev. Neurosci. *13*, 251–266. https://doi.org/10.1038/nrn3171.

Willard, A.M., Isett, B.R., Whalen, T.C., Mastro, K.J., Ki, C.S., Mao, X., and Gittis, A.H. (2019). State transitions in the substantia nigra reticulata predict the onset of motor deficits in models of progressive dopamine depletion in mice. Elife *8*, e42746. https://doi.org/10.7554/elife.42746.

Wilson, C.J., Chang, H.T., and Kitai, S.T. (1990). Firing patterns and synaptic potentials of identified giant aspiny interneurons in the rat neostriatum. J. Neurosci. *10*, 508–519. https://doi.org/10.1523/jneurosci.10-02-00508.1990.

Wolff, S.B.E., Gründemann, J., Tovote, P., Krabbe, S., Jacobson, G.A., Müller, C., Herry, C., Ehrlich, I., Friedrich, R.W., Letzkus, J.J., and Lüthi, A. (2014). Amygdala interneuron subtypes control fear learning through disinhibition. Nature *509*, 453–458. https://doi.org/10.1038/nature13258.

Xu, M., Chung, S., Zhang, S., Zhong, P., Ma, C., Chang, W.C., Weissbourd, B., Sakai, N., Luo, L., Nishino, S., and Dan, Y. (2015). Basal forebrain circuit for sleep-wake control. Nat. Neurosci. *18*, 1641–1647. https://doi.org/10.1038/nn.4143.

Yang, Y., Cui, Y., Sang, K., Dong, Y., Ni, Z., Ma, S., and Hu, H. (2018). Ketamine blocks bursting in the lateral habenula to rapidly relieve depression. Nature *554*, 317–322. https://doi.org/10.1038/nature25509.

Zemel, D., Gritton, H., Cheung, C., Shankar, S., Kramer, M., and Han, X. (2022). Dopamine depletion selectively disrupts interactions between striatal neuron subtypes and LFP oscillations. Cell Rep. *38*, 110265. https://doi.org/10.1016/j.celrep.2021.110265.

STAR★METHODS

KEY RESOURCES TABLE

REAGENT or RESOURCE	SOURCE	IDENTIFIER
Antibodies		
Rabbit anti-TH	Millipore	Cat #AB152; RRID: AB_390204
Alexa Fluor 594 Donkey anti-rabbit IgG (H + L)	Invitrogen	Cat #R37119; RRID: AB_2556547
Bacterial and virus strains		
rAAV2/9-TH-NLS-Cre	BrianVTA	Cat #PT-0179
rAAV2/9-Ef1α-DIO-hChR2(H134R)-mCherry	BrianVTA	Cat #PT-0002
rAAV2/9-Ef1α-DIO-mCherry	BrianVTA	Cat #PT-0013
rAAV2/9-Ef1a-DIO-eNpHR 3.0-EYFP	BrianVTA	Cat #PT-0006
rAAV2/9-EF1a-DIO-EYFP	BrianVTA	Cat # PT-0012
rAAV2/9-Ef1a-DIO-eNpHR 3.0-mCherry	BrianVTA	Cat #PT-0007
rAAV2/9-Ef1a-DIO-SwiChRca-EYFP	BrianVTA	Cat #PT-1438
rAAV2/9-Ef1a-DIO-ChETA(E123T/H134R)-EYFP	UPenn Vector Core	Cat #26968
Chemicals, peptides, and recombinant proteins		
DAPI	Vector Laboratories	Cat # H-1200; RRID: AB_2336790
Donkey serum	NQBB	Cat #A4016-37
Experimental models: Organisms/strains		
Mouse: C57BL/6J	Charles River	Cat #219
Mouse: Drd2-Cre	MMRRC	MMRRC_032108-UCD
Mouse: Drd1a-Cre	MMRRC	MMRRC_071264-UCD
Mouse: ChAT-IRES-Cre	Jackson Laboratory	JAX stock # 006410
Mouse: PV-IRES-Cre	Jackson Laboratory	JAX stock # 017320
Mouse: SOM-IRES-Cre	Jackson Laboratory	JAX stock # 013044
Software and algorithms		
OmniPlex Software	Plexon	Version 1.11.0
Offline Sorter	Plexon	Version 4.0.2
Neuroexplorer	Plexon	Version 5.215
Any-maze	Stoelting	Version 4.112
MATLAB	MathWorks	Version 2021b
Prism	GraphPad Software	Version 8.0.2
Code archived	This manuscript	https://doi.org/10.5281/zenodo.6732851
Other		
Optical power meter	Thorlabs	PM100D
Fluorescent confocal microscope	Zeiss	LSM700

RESOURCE AVAILABILITY

Lead contact

Further information and request for resources and reagents should be directed to and will be fulfilled by the lead contact, Dr. Wei Lu (luwei@seu.edu.cn).

Materials availability

This study did not generate new unique reagents.

Data and code availability

- All data reported in this paper will be shared by the lead contact upon request.
- All original code has been deposited at Zenodo and is publicly available as of the date of publication.

- Any additional information required to reanalyze the data reported in this paper is available from the lead contact upon request. DOIs are listed in the key resources table.

EXPERIMENTAL MODEL AND SUBJECT DETAILS

All animal breeding, care and experimental protocols had been approved by the Experimental Animal Ethics Committee of Southeast University. Mice were housed in groups of five and maintained on a 12 h light-dark cycle (starting at 7 a.m.) with ad lib access to standard food and tap water. All mice that participated in optogenetics and multichannel recording experiments and behavioral tests were adults (2-4 months old, male, singly housed). Strain types included in the experiments are as followed: C57BL/6 mice; Mice from MMRRC: Drd2-Cre (MMRRC_032108-UCD); Drd1a-Cre (MMRRC_071264-UCD); mice from Jackson Laboratory: ChAT-IRES-Cre (006410); PV-IRES-Cre (017320); SOM-IRES-Cre (013044). Drd1-cre mice were kindly provided by Professor Minmin Luo (National Institute of Biological Sciences), Drd2-cre mice were kindly provided by Professor Shengxi Wu (Air Force Medical University), SOM-IRES-Cre mice were kindly provided by Professor Fuqiang Xu (Wuhan Institute of Physics and Mathematics, CAS), ChAT-IRES-Cre mice and PV-IRES-Cre were kindly provided by Professor Peng Cao (National Institute of Biological Sciences). Mice were randomly assigned to experimental groups.

METHOD DETAILS

Virus preparation

rAAV2/9-TH-NLS-Cre (titre: 5.51×10^{12} v.g./ml, BrianVTA, Inc), rAAV2/9-Ef1α-DIO-hChR2(H134R)-mCherry (titre: 5.94×10^{12} v.g./ml, BrianVTA, Inc), rAAV2/9-Ef1α-DIO-mCherry (titre: 1.49×10^{13} v.g./ml, BrianVTA, Inc), rAAV2/9-Ef1a-DIO-eNpHR 3.0-EYFP (titre: 6.62×10^{12} v.g./ml, BrianVTA, Inc), rAAV2/9-Ef1a-DIO-eNpHR 3.0-mCherry (titre: 5.81×10^{12} v.g./ml, BrianVTA, Inc), rAAV2/9-Ef1a-DIO-SwiChRca-EYFP (titre: 6.54×10^{12} v.g./ml, BrianVTA, Inc), rAAV2/9-EF1a-DIO-EYFP (titre: 7.28×10^{12} v.g./ml, BrianVTA, Inc) and rAAV2/9-Ef1a-DIO-ChETA(E123T/H134R)-EYFP (titre: 5.87×10^{12} v.g./ml, UPenn Vector Core) were stored at −80°C.

Surgical procedures

Stereotaxic surgeries involved the injection of virus and placement of optical fibers and optrodes into the brain. To begin the surgeries, mice were first anesthetized with isoflurane oxygen mixture (induced 3%, maintained 1.5%) and placed on a stereotaxic system (RWD Instruments).

To selectively express opsins, we injected conditional Cre-dependent recombinant adeno-associated viruses (rAAV) into DS of PV-Cre, ChAT-Cre, SOM-Cre, Drd2-Cre or Drd1a-Cre mice, respectively. To express the excitatory channelrhodopsin-2 for optogenetic manipulations, we used rAAV-Ef1α-DIO-hChR2(H134R)-mCherry or rAAV-Ef1a-DIO-ChETA(E123T/H134R)-EYFP. For the expression of inhibitory halorhodopsins, we used an rAAV-Ef1α-DIO-eNpHR3.0-EYFP or rAAV2/9-Ef1a-DIO-SwiChRca-EYFP. Virus were delivered into the DS (AP 0.50mm, LM 1.40mm, DV 2.50–3.50mm) using pulled glass capillaries connected to a pressure microinjector (WPI Instruments). 250nL virus per mouse was delivered into the DS at a rate of 25 nL/min. In order to make dopaminergic neurons specifically express halorhodopsin, we mixed two viruses (THp-Cre and DIO-eNpHR3.0-EYFP) together and then injected the mixture into the SNc (AP -3.10mm, LM 1.40mm, DV 4.30mm). 150nL mixed virus were delivered into the SNc at a rate of 15 nL/min. The needle was left in place for 10 min post-injection. Afterwards the wounds were stitched and mice were placed in an incubator for recovery from anesthesia.

For optic fiber implantation, each fiber (Thinker Tech) was implanted 250μm above the viral injection site. The fiber was fixed to the surface of the skull with dental cement (GC INTERNATIONAL CORP.). For optrode implantation, a 32-channel customized optrode (see below) was implanted into the DS following a protocol similar to that of fiber implantation.

Optogenetic manipulation

Optogenetic operations were performed using a 200-μm, 0.22 NA fiber optic patch cord to deliver light to the implanted fibers. In order to ensure that the animals were free moving, the connected fiber optic patch cord were hung above the behavioral device. We used an optical power meter (PM100D, Thorlabs) to measure the light intensity before the experiment. In optogenetic manipulation, we adjusted the light intensity of the fiber tip to about 5mW. A 473-nm blue laser was delivered to mice expressing ChR2 and mCherry. The blue laser delivery paradigm was either 10 Hz, or 20Hz, or 40Hz per protocol. For mice expressing eNpHR3.0, the same set-up was used except that now a 593-nm yellow light laser was employed. The yellow light delivery paradigms included either a continuous light-on period for 15s or 1 min long phasic stimulation epochs separated by 1 min of no light protocol. For closed loop experiment, 593-nm yellow light was used for the photoinhibition of SNc DANs and 473-nm blue light was used to trigger the online optogenetic manipulation.

Optrode recordings and optogenetic identification of striatal neurons

In order to identify neurons expressing ChR2 or ChETA in the DS of free-moving mice, customized optrodes were used. Each optrode consisted of a 200-μm optical fiber and eight tetrodes. The tetrode was made by twisting four platinum-iridium wires (California Fine

Wire) into one. The tetrode wires were then plated with gold solution (Plexon Inc.) to modulate the impedance to 150 -300 kΩ. The tetrode wires were 0.2–0.3 mm longer than the optical fiber. The optrode was fixed on a microdrive array, allowing the optrode assembly to move vertically in search of light-sensitive neurons. We welded ground wires to screws on the surface of the skull as ground attachment. The optrode assembly was fixed to the skull with skull screws and dental adhesive. Then animals recuperated for 2 weeks before single-unit recording. Signals were collected using OmniPlex System (Plexon Inc.) controlled by OmniPlex Software. Spontaneous spiking activity was filtered at 0.25–5 kHz and digitized at 40 kHz sampling rate. LFP was filtered at 0-250 Hz and digitized at 1 kHz sampling rate. After each recording session, the tetrode was lowered for 70um (1 step). The mice would then recover for at least 48 h before next recording. When the signal recording was complete, the electrode tip locations and virus expression were reconstructed using standard histological procedures.

To identify PV+, ChAT+, SOM+, Drd2+ or Drd1a + neurons using optogenetics, we tested the response of all recorded neurons to light stimulation (Lima et al., 2009). We used blue light laser to activate ChR2 or ChETA (10 or 40 Hz, 10 ms per pulse, 60 pulses, 5 mW). If the response time delay of a neuron to light stimulation is less than 5 ms, we considered the neuron to be directly driven (Figure 2B). To ensure that spontaneous and light-induced spikes of identified neurons were from the same neuron, we calculated the waveform similarity between spontaneous and light-induced spikes of all identified neurons. We used the correlation coefficient to quantify the similarity between spontaneous and light-induced spikes. Only activities with correlation coefficient greater than 0.95 were considered as stemming from the same neuron. (Figure 2C). Optogenetically identified spikes were then clustered using three parameters related to the spike asymmetry, the valley FHWM, and the length of peak1-to-peak2 to discriminate striatal interneurons. dMSNs and iMSNs were distinguished by using parameters as followed: the length of peak1-to- valley, the valley FHWM, and the length of peak1-to-peak2.

Spike sorting

Neural data were sorted by using Offline Sorter V4 (Plexon Inc.) as previously described (Lima et al., 2009). We clustered the waveforms based on principal components analysis (PCA) as previously described (Anikeeva et al., 2011; Wolff et al., 2014). A set of waveforms were considered to be produced by a single cell if it displayed a definite refractory period (>1 ms) in the autocorrelogram and formed a discrete cluster distinct from clusters of other units. Sorted waveforms were then stored for further analysis. Neuronal activities were denoted by either frequencies or Z-score values (Wolff et al., 2014).

Data analysis

Data analysis were performed using Neuroexplorer5 (Plexon Inc.) and MATLAB. LFPs were low-pass filtered from 1 to 250 Hz using a fourth-order Tchebyscheff filter. All spectral analysis was done using multitaper Fourier transform. We calculated the power spectrum of LFP by using the mtspecgram function of the Chronux toolbox (Bokil et al., 2010). The final power spectrum was calculated by first averaging results from all electrodes from each animal and then averaging results from all animals.

Spike-field coherence (SFC) measured the synchronization between local field potential and spikes. The SFC was computed as the ratio of the frequency power spectrum of the STA (spike-triggered average) over the mean frequency spectrum of the LFP traces. To calculate STAs, we averaged LFPs within a window of ±300 ms centered on each trigger spike. We only used LFPs and spikes recorded from different tetrodes for subsequent analysis. We used the multitaper analysis with seven tapers to measure the spectrum of the STA (fSTA). For this purpose, we used the Chronux Toolbox (Chronux 2.0). The average spectrum of the LFP traces resulted in the spike triggered power (STP).

In order to investigate the real-time phase relationships between spike and LFPs at specific frequency bands (Garas et al., 2016; Nakamura et al., 2014; Sharott et al., 2012), we estimated the phase of each spike at specific frequency by using the continuous wavelet transform. The phase was between −180° and 180°, phase zero equal to the valley and phases −180° and 180° equal to the peak of the oscillation.

Behavioral assays

All behavioral tests were performed on male mice between 12 and 16 weeks old. For acclimations, mice were handled for 5 consecutive days (5 min/day) before the experiment. Mice were placed in the center of the open-field box (40 cm × 40 cm × 40.5cm) at the beginning of the test and allowed to move freely for 5 min for acclimation to the environment. A camera was fixed above the chamber to record the behavior of each animal (Any-maze, Stoelting). For DANs photoinhibition manipulations, mice were placed in the open field and yellow light was delivered continuously for 15 s. For SOMs photoinhibition manipulations, mice were placed in the open field and irradiated with yellow light for 10 min (1 min long phasic stimulation epochs separated by 1 min of no light). During ChATs or iMSNs photoactivation manipulations, mice were able to move freely throughout the chamber and blue light was delivered for periods of 5 min (20Hz, 10 ms per pulse).

Anatomical verification

Animals were anaesthetized with isoflurane and then perfused transcardially with phosphate-buffered saline (PBS), followed by 4% paraformaldehyde in PBS. We placed brains in 4% paraformaldehyde overnight for post-fixation and in 40% sucrose in PBS for equilibration. Brains were coated with Tissue-Tek OCT compound (SAKURA Inc.) and then frozen at −80°C. Brains were sectioned coronally in 35-μm slices by using freezing microtome (CM1950, Leica) and kept in PBS solution at 4°C before mounting. Then slices

were DAPI (H-1200, Vector Laboratories) stained and carefully examined (Figure S2). A fluorescent confocal microscope (Zeiss, LSM700) was employed for imaging.

Immunofluorescence

To test specificity of combined viruses (THp-Cre and DIO-eNpHR3.0-EYFP), we calculated the co-localization of the fluorescent label transduced by the virus and the corresponding immunofluorescence (IF). We used the experimental protocol as previously described for immunofluorescence detection of TH (Anikeeva et al., 2011; Stauffer et al., 2016). We paraformaldehyde fixed and sectioned 35-μm-thick brain slices using protocols as described above. We washed slices twice with PBS for 10 min and blocked with blocking solution (10% donkey serum (NQBB, A4016-37) in PBST (PBS containing 3‰ Triton-X-100) for 2h at 20°C. Next the slices were incubated with primary antibodies (rabbit anti-TH, Merck Millipore, AB152, 1:1000) overnight at 4°C. The slices were washed thrice with PBS for 10 min and incubated with fluorescent secondary antibodies (Alexa Fluor 594 for Donkey anti-rabbit IgG (H + L), Invitrogen, R37119, 1:200) for 2 h at 20°C. The slices were last washed thrice with PBS and then coverslipped with Mounting Medium containing DAPI. We used ImageJ (National Institutes of Health) to manually count virus-labeled cells, IF-labeled cells and neurons co-labeled with the two.

Closed-loop optogenetic intervention

Physiological data from OmniPlex system (Plexon Inc.) was analyzed for real-time processing of LFP in MATLAB by customized program scripts and software development kit MatlabClientDevelopKit (Plexon Inc.).

The wide-band signal was bandpass-filtered (12–25 Hz), and then filtered LFPs were calibrated and smoothed using a moving average filter with a 400-millisecond duration to produce online beta amplitude values. The amplitude value was used to trigger stimulation via a self-defined threshold by a digital output application program PlexonDo (Plexon Inc.). The trigger output was onset when the amplitude of more than four channels is higher than given threshold. The delay from exceeding the threshold to the start of stimulation is 30–40 milliseconds. Once the stimulus is triggered, it would continue until the beta amplitude is below the threshold again. The program provided a continuous readout of the stimulus state. As a control, random stimuli were presented at random intervals under the constraints of the same stimulation duration.

QUANTIFICATION AND STATISTICAL ANALYSIS

The number of animals used in our experiment was comparable to other studies using similar techniques and animal models. Statistical analyses were calculated using GraphPad Prism software v8. All statistical tests were two-tailed. Differences were considered significant when $p < 0.05$. We used the D'Agostino & Pearson omnibus normality test to detect normality between group samples and used the Brown–Forsythe test to assess equal variances between group samples. When the sample conformed to the normal distribution or the variance was homogeneous, paired student's t-test, or unpaired student's t-test were used. Where normality or equal variance of samples failed, Wilcoxon matched-pairs signed rank test, or Mann Whitney test were used, respectively. We performed the Rayleigh test for assessment of circular uniformity. We used the 'circ_rtest' function to evaluate if the spike unit activity is uniformly distributed across the β-oscillation cycles (H0, $p > 0.05$). If H0 was rejected, striatal neuron was considered as significantly phase locked to beta oscillations. Statistical details of experiments are described in method details or Figure Legends.